Article

In Vivo Photoacoustic/SPECT Imaging for Dynamic Monitoring of Aggregation-Enhanced Photothermal Nanoagents

Yangyun Wang, Ziling Sun, Zhizhong Chen, Yanxian Wu, Yuan Gu, Subin Lin, and Yong Wang

In Vivo Photoacoustic/SPECT Imaging for Dynamic Monitoring of Aggregation-Enhanced Photothermal Nanoagents

Yangyun Wang,[†,┬] Ziling Sun,[‡,┬] Zhizhong Chen,[§] Yanxian Wu,[†] Yuan Gu,[†] Subin Lin,[§] Yong Wang[†,*]

† State Key Laboratory of Radiation Medicine and Protection, School for Radiological and Interdisciplinary Sciences (RAD-X), Collaborative Innovation Center of Radiation Medicine of Jiangsu Higher Education Institutions, Soochow University, 199 Renai Road, Suzhou Industrial Park, Suzhou 215123, China

‡ Department of Biochemistry and Molecular Biology, School of Biology & Basic Medical Sciences, Soochow University, 199 Renai Road, Suzhou Industrial Park, Suzhou 215123, China

§ Department of Orthopedic, the Second Affiliated Hospital of Soochow University, 1055 Sanxiang Road, Suzhou 215004, China

ABSTRACT: Emerging nanomedical strategy is to construct a nanoagent that affords not only diagnostic and therapeutic functions, but also imaging-guided treatment. It is crucial to understand the in vivo biological processes of nanoagents for improving theranostic function and biosafety. Herein, we report a multimodal photoacoustic/SPECT imaging technique to dynamically monitor the in vivo behaviors of nanoagents. Near-infrared cypate-induced silk fibroin nanoassembly is chose as the object of nanoagents due to their promise in biocompatibility and aggregation-enhanced photothermal effect. This unique effect makes the nanoagents useful for the integration of photoacoustic imaging and photothermal therapy. Moreover, the nanoagents are also labeled with the radionuclides (^{99m}Tc) to render SPECT imaging. Multimodal photoacoustic/SPECT imaging provides real time, noninvasive, sensitive, and whole-body 3D information about nanosgents' distribution in vivo. These results highlight the significance of visualizing the in vivo behaviors of nanoagents and locating the tumor in vivo, substantially benefiting the better treatment planning.

Theranostic nanoagents integrated with diagnostic and therapeutic functions hold great promise in tumor imaging-guided therapy to enhance treatment efficacy.[1] It is very important to fully understand the dynamic process (e.g. absorption, distribution, metabolism, and excretion) of theranostic nanoagents for in vivo applications.[2] However, the current analytical methodologies are difficult to provide dynamic, noninvasive, and whole-body 3D information about nanosgents' distribution due to the highly complicated nano/bio interface interactions.[3] Imaging-based analytical techniques would offer great convenience to visualizing the in vivo behaviors of nanoagents in real time.[4-6] While multimodal imaging combined with the advantages of different imaging technologies can accurately analyze the biological dynamic processes, and thus more sensitively locate tumor for efficient treatment planning.[7-9]

In various imaging technologies, photoacoustic imaging (PAI) is a burgeoning technique that bridges the high sensitivity of optical imaging with the high spatial resolution of ultrasound.[10] PAI employs photoabsorbing agents to generate photothermal conversion effect from short laser pulses, a rapid thermoelastic expansion of tissue can result in the generation of a wide-band ultrasound wave.[11] So the PAI probes have generally been used as photothermal therapy (PTT) to construct the theranostic agents.[12] Nevertheless, PAI can only achieve a penetration depth of several centimeters even in near-infrared (NIR) windows.[9] Furthermore, single-photon emission computed tomography (SPECT) imaging, as a nuclear imaging technology, can sensitively detect the 3D

spatial distribution of γ-ray emitting radionuclides within the wholebody but not limited by the tissue depth.[7] SPECT therefore constitute orthogonal complements to PAI, and combining these techniques can accurately focus on the tumor area with high resolution and high sensitivity. This strategy is embodied in the single probe with PAI/SPECT multimodal functionality, including asialoglycoprotein receptors targeted multimodal imaging in liver diseases,[13] and ultrasmall nanoagents for multimodal imaging-guided radio-photothermal synergetic therapy.[14]

Herein, we propose an indocyanine green (ICG) analogue cypate-induced silk fibroin self-assembly (Cy@Silk) nanoagents for in vivo multimodal theranostic application. In this assembly nanostructure, silk fibroin originated from *Bombyx mori silkworm cocoons* is emerging as a promising nanocarrier for for loading imaging and therapy agents.[15, 16] Like other protein-based theranostic nanoagents,[17, 18] hydrophobic dye-induced self-assembly strategies can improve their biocompatibility and chemical stability for in vivo applications. The high aggregation densities of dye in the assembly lead to extreme self-quenching effect and high light absorption efficiency. Therefore, unlike the fluorescent dye monomer,[19] the unique assembly has higher photothermal conversion efficiency and was an excellent PAI/PTT agent. After labeling radionuclides (^{99m}Tc), the dynamic biodistribution processes of Cy@Silk nanoagents in vivo were tracked in real time by photoacoustic and SPECT imaging. More importantly, ^{99m}Tc labeled Cy@Silk nanoagents could be used for in vivo photoacoustic and SPECT imaging of

osteosarcoma, followed by photothermal therapy for imaging navigation. The design strategy of this work is schematically illustrated in **Scheme 1**.

Scheme 1. Schematic Illustration of Fabrication of ^{99m}Tc-Labeled Silk-Assembly Theranostic Nanoagents (A) and *In Vivo* Dynamic Photoacoustic/SPECT Imaging and Photothermal Imaging/Therapy of Osteosarcoma (B).
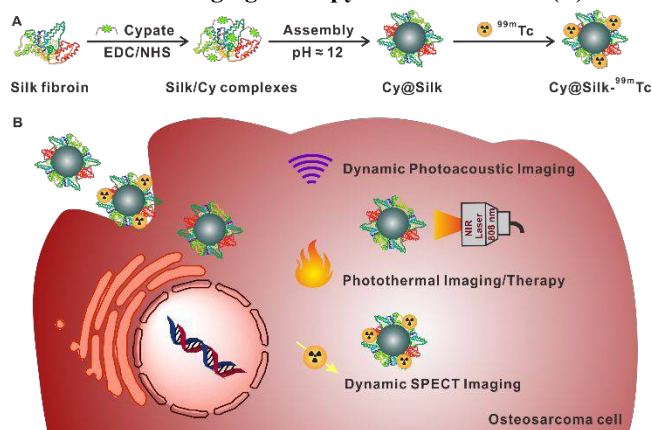
EXPERIMENTAL SECTION

Materials and Chemicals. *Bombyx mori* silkworm cocoons were provided by National Engineering Laboratory for Modern Silk of Soochow University. [99m]Tc pertechnetate ([99m]TcO$_4^-$) was obtained from GMS (Shanghai, China). All other chemicals were obtained from Aladdin (Shanghai, China).

Instrumentation and Characterization. The morphology of Cy@Silk was characterized using a transmission electron microscope (Tecnai G2 spirit BioTwin, FEI). Dynamic light scattering (Zetasizer ZS90, Malvern) was used to measure the hydrodynamic size. The fluorescence and absorbance spectrum were measured using fluorescence spectrophotometer (FLS 980, Edinburgh) and UV-Vis-NIR spectrophotometer (Lambda 35, PerkinElmer). PAI and SPECT imaging was performed using MSOT INVISIO-256 (IThera Medic) and U-SPECT+/CT (MILABS), respectively. The photothermal imaging was captured via a thermal infrared camera (A65, FLIR).

Synthesis of Cy@Silk Nanoagents. The silk fibroin solution was prepared according to the literature.[20] The carboxyl group of the cypate is coupled to the amino group of silk fibroin by carbodiimide-catalyzed amide reaction,[21, 22] and then the above solution was stirred at 37 °C for 12 h under the conditions of pH 12. The obtained solution was dialyzed to form self-assembled Cy@Silk nanoparticles with hollow fibre dialysis membrane, (50 kDa). To prepare radiolabeled nanoparticles, 10.0 μL of fresh SnCl$_2$ solution (1.0 mg mL^{-1}, pH ≈ 3) was mixed with 0.2 mL Cy@Silk (50 μg mL^{-1}) solution, and then 0.5 mL [99m]TcO$_4^-$ (1.2 mCi) solution was immediately added into the mixture and reacted for 10 min. The ^{99m}Tc-labeled Cy@Silk solution was purified by ultrafiltration centrifugation (Ultrafree-PF filters, 100 kDa, Millipore). The product obtained was named Cy@Silk-^{99m}Tc, and its radiochemical purity is as high as 95%.

In Vitro Photothermal and Photoacoustic Effect. To evaluate the photothermal effect, Cy@Silk solutions were irradiated at the concentration of 0, 25, 50, 100, and 200 μg mL^{-1} using a 808 nm laser (0.75 W cm^{-2}) for 10 min, and the photothermal heating curve was recorded by a thermal infrared camera (A65+, FLIR). The photothermal conversion efficiency of nanoparticles was calculated according to the literature.[14] For *in vitro* photoacoustic imaging of Cy@Silk solution in different concentrations, the excitation wavelength of 680 nm was adopted. Photoacoustic signal intensities were measured by region of interest (ROI) analysis using the MSOT imaging system software package. For photothermal cytotoxicity, K7M2 cells (murine osteosarcoma cells) were incubated with different concentrations of Cy@Silk nanoparticles and then irradiated with 808-nm laser (0.75 W cm^{-2}) for 10 min. After 24 h, methyl thiazolyl tetrazolium (MTT) assay was used to evaluate the cell viability.

Animal Experiments. All animal experiments were approved by Animal Ethics Committee of Soochow University (Suzhou, China). The orthotopic osteosarcoma model was established using the 4-week-old female BALB/c mice based on the literature.[22, 23] All animal experiments were performed under anesthesia with 2.5% isoflurane.

In Vivo Multimodal Imaging. For visualization of dynamic process of nanoagents, the normal mice were intravenously administered with 200 μL Cy@Silk (50 μg mL^{-1}) or 200 μL Cy@Silk-[99m]Tc (800 μCi ^{99m}Tc). A series of PAI and SPECT/CT images were captured at pre-injection or other time point of post-injection. For in vivo tumor locating, 200 μL Cy@Silk solution (50 μg mL^{-1}) or 200 μL Cy@Silk-[99m]Tc (800 μCi ^{99m}Tc was intravenously injected into the mice bearing osteosarcoma. At pre-injection (Pre), or 30 min, 2 and 24 h post-injection, a series of PAI and SPECT/CT images were captured.

In Vivo Infrared Thermography. For *in vivo* infrared thermography, the mice bearing osteosarcoma were intravenously injected with 50 μg mL^{-1} Cy@Silk nanoagents. At 6 h post-injection, the tumor was irradiated with an 808-nm laser (0.75 W cm^{-2}) for 5 min, while the thermal imaging was monitored during the irradiation period.

In Vivo Anticancer Efficacy, and Pathologic Analysis. To test the prediction that a single dose of 50 μg mL^{-1} (200 μL) could destroy tumors under the NIR laser irradiation, the mice bearing osteosarcoma (approximately 60 mm^3) were intravenously injected with either Cy@Silk or PBS. Thirty mice were divided into four groups for NIR laser irradiation, such as PBS only treated mice (group 1, PBS), Cy@Silk only treated mice (group 2, Cy@Silk), saline treated mice with NIR laser irradiation (group 3, PBS + NIR), Cy@Silk treated mice with NIR laser irradiation (group 4, Cy@Silk + NIR). Irradiation conditions were as follows: the power density was 0.75 W cm^{-2} and irradiation time was 5 min. Then, the tumor volume (V) was measured every other day by the following formula: V= L×W^2/2, where W and L refer to the width and length of the tumor, respectively. Relative tumor volume, which was the ratio of real-time tumor volume to initial tumor volume, was used to monitor tumor growth. To further evaluate the *in vivo* therapy against tumor, one of each group was sacrificed and the tumor was removed for histopathological analysis at 12 h post-irradiation. Subsequently, the tumors were frozen and cut into the sections with the thickness of 10 μm, and then stained with haematoxylin & eosin (H&E). The stained slices were observed using an brightfield microscopy (IX73, Olympus). Finally, the mice were sacrificed under anesthetic status after the experiments.
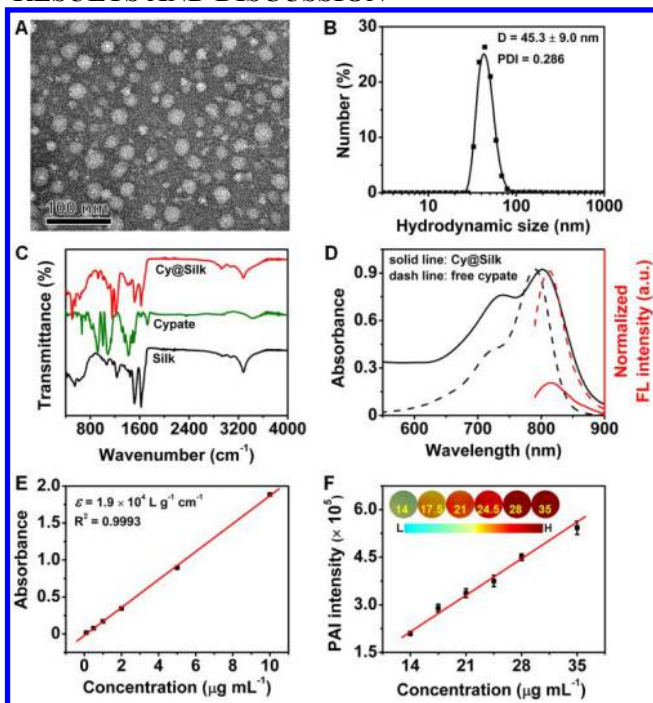
RESULTS AND DISCUSSION

Figure 1. (A) TEM of Cy@Silk nanoparticles; (B) DLS of Cy@Silk nanoparticles; (C) FT-IR spectrum of Cy@Silk nanoparticles, free cypate and silk; (D) Absorbance and fluorescence spectrum of Cy@Silk nanoparticles and free cypate; (E) Molar absorption coefficient of Cy@Silk nanoparticles; (F) Concentration-dependent PAI signal (inset: PAI signals corresponding to different concentrations).

Synthesis and Characterization of Cy@Silk Nanoagents. Near-infrared fluorescent dye cypate is an analog of FDA-approved ICG.[19] Unlike ICG lacking reactive groups, cypate with dicarboxy groups can be directly conjugated to other molecules by a succinimide linkage.[21, 22] In this article, the cypate molecule was covalently bound to the amine groups of silk fibroin, the complexes then formed nanoparticles (Cy@Silk) by self-assembly under alkaline conditions (Scheme 1A). The size of nanoparticles is uniform with an average of about 18.9 nm in the TEM image (Figure 1A and Figure S1 in the Supporting Information). However, DLS shows that the nanoparticles have a hydrodynamic diameter of 45.3 nm due to the negative potential and stretch of surface silk fibroin (Figure 1B and Figure S2 in the Supporting Information). FT-IR spectroscopy also confirms the presence of silk on the surface of nanoparticles in the fingerprint region of ~1600 nm (Figure 1C). It is worth noting that Cy@Silk nanoparticles exhibit an excellent colloidal stability in the water and physiological solution (Figure S3 in the Supporting Information).

After self-assembly, the fluorescence of cypate is drastically quenched due to the high aggregation density in the Cy@Silk nanoparticles (Figure 1D). The result indicates that the excited state of Cy@Silk nanoparticles return to their ground state via non-radiative transitions instead of photon emission. Based on this fact, Cy@Silk nanoparticles have a 100 times larger molar absorption coefficient compared to the free dye (Figure 1E).[24] Meanwhile, Cy@Silk nanoparticles also exhibit strong concentration-dependent photoacoustic signals (Figure 1F). The results indicate that Cy@Silk nanoparticles with strong NIR absorption can be used as a potential PAI agent.

Similarly, the photothermal effect of Cy@Silk nanoparticles also shows irradiation time and concentration-dependent properties. With the gradual increase of concentration and the prolongation of irradiation time, the photothermal signal is getting stronger and stronger (Figure 2A), and the photothermal temperature is gradually increasing (Figure 2B). After 5 min of irradiation with the 808-nm laser (0.75 W cm^{-2}), the enhanced temperature raises 43 $^{\circ}$C at a concentration of 20 μg mL^{-1}. Due to the compact self-assembled nanostructures, the Cy@Silk nanoparticles have a photothermal conversion efficiency of 46.5 % (Figure 2C), that of the free dye is only 3.37 %.[25] Next, we examined the photothermal imaging of cells after endocytic nanoparticles. Different concentrations of nanoparticles were incubated with the K7M2 cells for 24 h, and then the cells were washed and irradiated with a power density of 0.75 W cm^{-2} for 5 min (Figure 2D). We found that the higher the concentration, the more obvious the photothermal signal, which may be due to the higher endocytosis effect at the high concentration. These results suggest that the nanoparticles are promising for PTT of tumors, as tumor cells can be killed by being kept at > 45 °C for several minutes.[26]
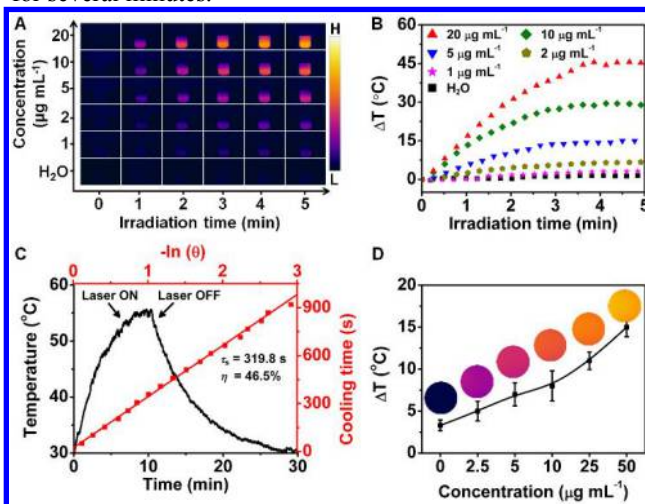

Figure 2. (A) Irradiation time and concentration-dependent photothermal signal for Cy@Silk nanoparticles; (B) Irradiation time and concentration-dependent photothermal temperature curves for Cy@Silk nanoparticles; (C) Temperature profile (black) of Cy@Silk nanoparticles (10 μg mL^{-1}) irradiated by 808-nm laser (0.75 W cm^{-2}) for 10 min, followed by natural cooling for calculating the photothermal conversion efficiency (η = 46.5 %). The linear fitting (red) of time from the cooling period versus negative natural logarithm of driving force temperature; (D) Photothermal imaging of cells incubated with different concentrations of nanoparticles.

In Vitro Cytotoxicity and PTT Effect. Considering the excellent photothermal performance of Cy@Silk nanoparticles for tumor ablation, in vitro cytotoxicity and PTT effect were further investigated. The cytotoxicity was evaluated by MTT assay, live/dead cell staining, and flow cytometry on the proliferation of K7M2 cells. Figure 3A shows that self-assembled nanoparticles effectively improve the biocompatibility of free dye. At a dye concentration of 100 μg mL^{-1}, the cell viability of the free dye is only 25%, while the nanoparticles are still as high as 100 %. The cytotoxicity of free dye is due to instability in water (Figure S4 in the Supporting Information).

To verify their photothermal ablation of tumor cells, K7M2 cells were incubated with different concentrations of Cy@Silk nanoparticles and then irradiated with 808-nm laser (0.75 W cm^{-2}) for 10 min. After 24 h post-irradiation, MTT assay shows that nanoparticles have a good photothermal ablation effect, and the cell viability is reduced to 20 % (Figure 3A). Visually, live/dead cell staining clearly indicates that most K7M2 cells were killed (red fluorescence) after incubation with 80 µg mL^{-1} Cy@Silk nanoparticles and exposed to irradiation with an 808 nm laser (Figure 3B). Conversely, the K7M2 cells have almost no damage in PBS, laser only, and the Cy@Silk nanoparticles only groups (green fluorescence).

Flow cytometry also confirmed the above results (Figure 3C), the K7M2 cells were treated with different concentrations of Cy@Silk nanoparticles and/or no NIR irradiation. Compared with the no NIR irradiation group, the PTT effect of Cy@Silk nanoparticles can more significantly induce K7M2 cells late apoptosis/necrosis, and exhibit significant concentration dependence. At 25 µg mL^{-1} of Cy@Silk nanoparticles with PTT, the proportion of apoptosis and necrotic cells is 45.69 % and 39.38 %, respectively. When the concentration is doubled, the necrotic cells are up to 81.36 %. These results indicate that the Cy@Silk nanoparticles have good biocompatibility and excellent photothermal ablation performance.
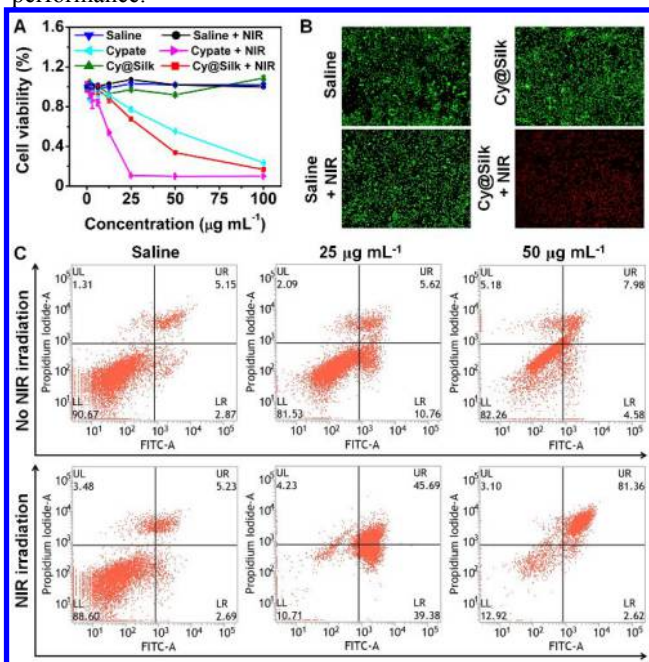

Figure 3. (A) The cytotoxicity of saline, free cypate, and Cy@Silk nanoparticles with or without NIR irradiation; (B) The live/dead cell staining of saline and Cy@Silk nanoparticles with or without NIR irradiation; (C) Flow cytometry of saline and different concentrations of Cy@Silk nanoparticles with or without NIR irradiation.

In Vivo Dynamic Distribution Tracking by Photoacoustic/SPECT Imaging. Derive from the excellent photoacoustic and photothermal performance in vitro, Cy@Silk nanoparticles can be potentially used as a theranostic agent for in vivo application. Undoubtedly, their theranostic functions and biosafety in vivo must be dominated by the fundamental biological processes.[27] Ideal theranostic nanoagents should be effectively cleared out of the body, have a good biocompatibility, and show minimum interference with

accurate theranostic applications.[28] So, we employed a multimodal SPECT/photoacoustic imaging technology for 3D dynamic monitoring of Cy@Silk nanoagents. In view of the high photothermal conversion efficiency of Cy@Silk nanoagents in NIR region, they have also been investigated as a PAI probe. For in vivo PAI, the 3D whole body image of a normal mouse was firstly captured at pre-injection. Then, 200 µL Cy@Silk nanoagents (50 µg mL^{-1}) solution was intravenously injected into the normal mice for real time imaging. As shown in Figure 4A, Cy@Silk nanoagents are mainly distributed in the bloodstream in the initial phase, and then they are gradually accumulated in aorta and reticuloendothelial phagocytic system (e.g. liver and spleen). To better understand the clearance pathways, liver section and kidney section images were also extracted, which are the two most important metabolic organs.[27] We found that the signal of liver continually increased in 8 h post-injection, then gradually decreased after 12 h post-injection. Contrast to kidneys, the PAI signal obviously increase in 4 h post-injection, and then gradually decrease. The results suggest the Cy@Silk nanoagents are mainly excreted from liver over a long period.

In addition to PAI, the multifunctional groups (e.g. –COOH, –NH$_2$ and –SH) on the surface of Cy@Silk nanoagents provide a good opportunity to fabricate the multimodal imaging probe. Thus, clinically metal radionuclide, ^{99m}Tc (half-life, $t_{1/2}$ = 6.02 h, γ-ray energy, E_γ = 140 keV),[14] can be chelated with the Cy@Silk nanoagents for SPECT imaging. 200 µL ^{99m}Tc labeled Cy@Silk nanoagents (i.e. Cy@Silk-^{99m}Tc nanoagents, 500 µCi ^{99m}Tc, 50 µg mL^{-1}) solution were intravenously injected into the normal mice for real time imaging (Figure 4B). Similar to in vivo PAI, SPECT imaging also indicate that Cy@Silk-^{99m}Tc nanoagents are circulated from the heart to metabolic organs. Carotid blood vessels and heart can be obviously distinguished within 2 h post-injection. During this time, the kidneys, especially the bladder, also showe strong signal. Since then, the signals of these organs have gradually decreased. The signal from liver and intestines is gradually increasing. After 24 h post-injection, the signal of these two organs still exist despite significantly decrease. In brief, both techniques confirmed that the main removal pathway of Cy@Silk nanoagents is from the liver through the gallbladder and intestines, and finally the feces. But more importantly, dynamic imaging results also show that the ^{99m}Tc labeled Cy@Silk nanoagents have excellent chemical stability in the body.

Recently, it is essential for quantitative analysis of the in vivo dynamics of nanoagents for understanding their biological effects. For example, we firstly monitor the dynamic changes of nanoagents in blood circulation. For the blood circulation half-life (Figure 4C), 200 µL Cy@Silk-^{99m}Tc nanoagents (50 µCi ^{99m}Tc, 50 µg mL^{-1}) solution were intravenously injected into the normal mice. At the fixed-point times, blood was collected from the eye socket, and monitored by a γ counter. The measured results indicate that the nanoagents exhibit a two-compartment pharmacokinetic behavior ($t_{1/2\alpha}$, 0.27 h and $t_{1/2\beta}$, 0.043 h). The short blood half-life is beneficial for rapid metabolism of nanoagents.[29] Of course, we also quantify the nanoagents in the two major organs involved in metabolism based on the photoacoustic/SPECT imaging, such as liver and kidneys. Quantitative results show that the liver signal has a peak at 4 h post-injection, which is about 3-4 times of that at pre-injection.
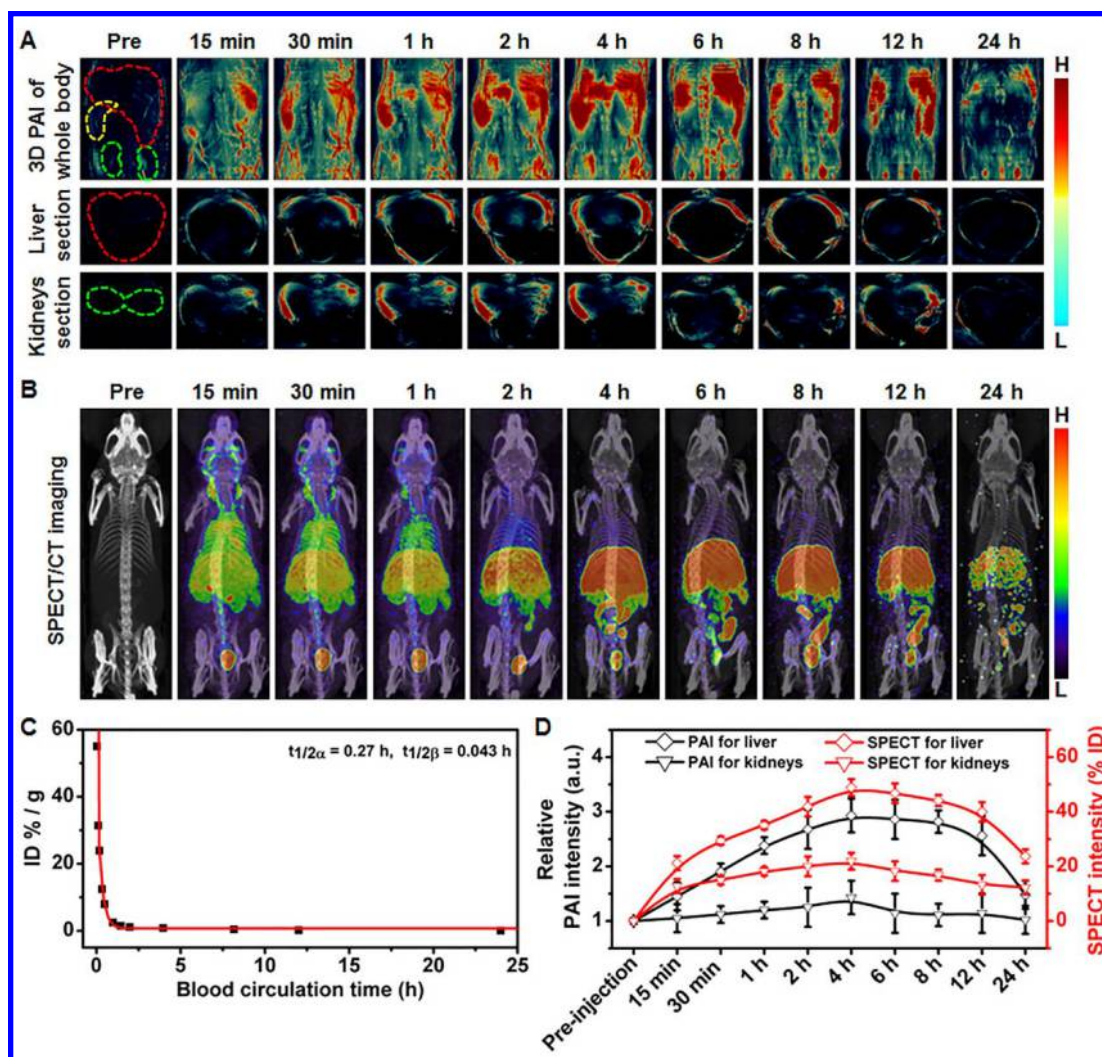
Figure 4. (A) In vivo real-time visualization of Cy@Silk nanoagents by 3D PAI. The principal organs regions are pointed by the dotted circle (red, yellow and green color stands for liver, spleen and kidney, respectively). (B) In vivo real-time visualization of Cy@Silk-[99mTc] nanoagents by SPECT/CT imaging. (C) Blood clearance profile of Cy@Silk-[99mTc] nanoagents in Balb/c mice. (D) Quantitative analysis of liver kidneys involved in metabolism based on the photoacoustic/SPECT imaging.
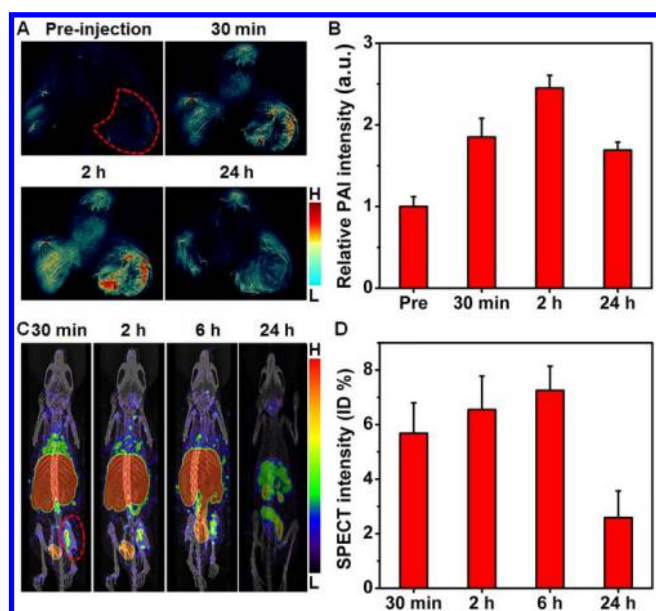

Figure 5. (A) In vivo PAI of mice bearing osteosarcoma with Cy@Silk nanoagents at pre-injection and 30 min, 2 and 24 h post-injection; (B) The PAI intensity of tumor section at different time points; (C) In vivo SPECT imaging of mice bearing osteosarcoma with Cy@Silk-[99mTc] nanoagents at 30 min, 2, 6 and 24 h post-injection; (D) The SPECT intensity of tumor region at different time points. The tumor region is pointed by the red dotted circle.

In Vivo Photoacoustic/SPECT Imaging of Tumor. To achieve efficient treatment of living tumors, accurate tumor imaging is essential. For in vivo PAI, 200 μL Cy@Silk nanoagents (50 μg mL^{-1}) solution were intravenously injected into mice bearing osteosarcoma. As shown in Figure 5A, PAI of tumor sections were captured at pre-injection and 30 min, 2 and 24 h post-injection. After 30 min post-injection, the photoacoustic signal has a significantly enhancement in the tumor area by enhanced permeability and retention (EPR) effect.[23, 30] As the peak, 4.3-fold enhancement appears at 2 h post-injection comparision with pre-injection (Figure 5B). It is worth noting that the nanoparticles are still accumulating in the tumor after 24 h post-injection. The results indicate that the Cy@Silk nanoagents have excellent in vivo cycle time and tumor enrichment efficiency, which is highly beneficial for subsequent in vivo PTT of tumor.[21]

For SPECT imaging, 200 μL Cy@Silk-^{99m}Tc Nanoagents, (500 μCi ^{99m}Tc, 50 μg mL^{-1}) solution were intravenously injected into mice bearing osteosarcoma. SPECT imaging was performed consecutively at 30 min, 2, 6 and 24 h post-injection. The SPECT images demonstrate high uptake of Cy@Silk-^{99m}Tc nanoagents in the tumor area via EPR effect, which is well consistent with the PAI (Figure 5C). In addition, SPECT signal is consistent with the dynamic distribution tracking in vivo. The further SPECT quantitative analysis provides accurate quantitative assessment of Cy@Silk-^{99m}Tc nanoagents uptake in tumor Figure 5D). The above results indicate that the Cy@Silk nanoagents can be as an excellent multimodal imaging probe with tumor targeting, and the nanoagents are very stable and biocompatible in the body.
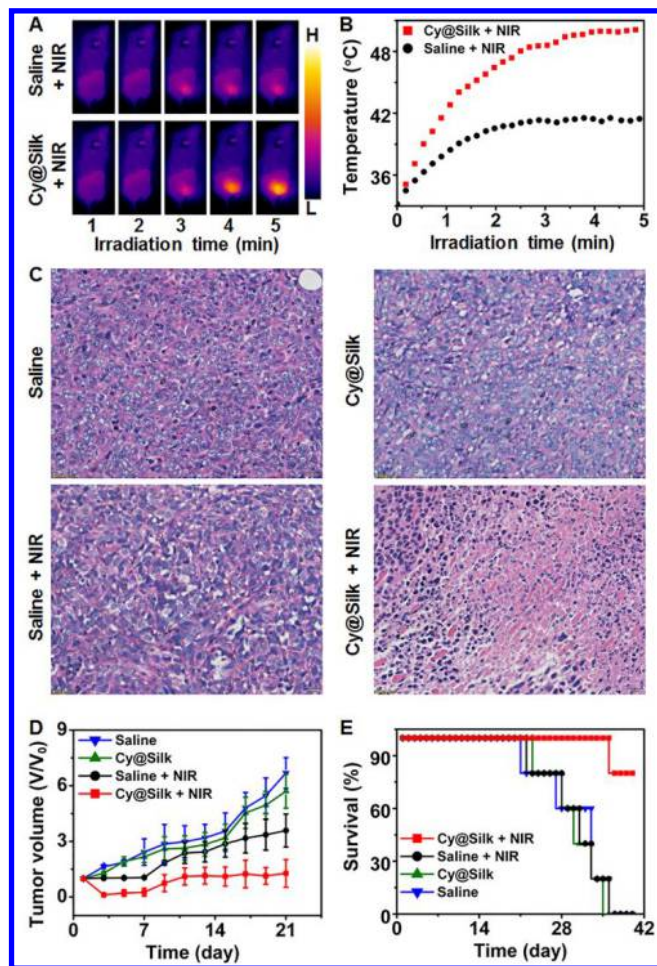

Figure 6. (A) The full-body thermal imaging of BALB/c mice bearing osteosarcoma intravenously injected with saline and Cy@Silk nanoagents (50 μg mL^{-1}) after an 808 nm laser (1 W cm^{-2}) irradiation for 0, 1, 2, 3, 4 and 5 min; (B) The tumor temperature variation in the Saline + NIR group and Cy@Silk + NIR group as a function of the irradiation time; (C) H&E staining of osteosarcoma in the all groups after 24 h of treatment; (D) The relative osteosarcoma growth volumes in the all groups as a function of the treatment time, V represents the real-time volume, and V_0 represents the initial volume; (E) The survival rates in the all groups as a function of the treatment time.

In Vivo Photothermal Therapy of Osteosarcoma. Encouraged by in vitro photothermal ablation and tumor targeting efficiency aforementioned, we further investigated in vivo PTT of osteosarcoma. In detail, BALB/c mice bearing osteosarcoma were intravenously injected with 200 μL saline or Cy@Silk nanoagents (50 μg mL^{-1}), and then the tumor site was irradiated with 808-nm laser (0.75 W cm^{-2}) for 10 min. As the multimodal imaging results show that the imaging signal of the tumor site in the mouse has a peak at 2 h post-injection, the mice were irradiated at this time point. These two groups ($n = 5$) are simply referred to as Saline + NIR group, and Cy@Silk + NIR group. As the control experiment, the other two groups of mice ($n = 5$) were injected with the same dose of the saline and Cy@Silk nanoagents, but not irradiated. Once irradiated with 808 nm laser, the full-body thermal images for monitoring the temperature variation was captured with a thermal infrared camera. As shown in Figure 6A, the tumor temperature is dramatically increased for Cy@Silk + NIR group contrasting to the Saline + NIR group. After 5 min of irradiation, the temperature of tumor region can increase to 54 °C, while the Saline + NIR group only increase to ≈ 40 °C (Figure 6B). Such high temperature are sufficient to ablate osteosarcoma cells and suppress malignant proliferation.[31] Pathological section analysis of tumor can confirm the inference. After 24 h of treatment, one mouse was sacrificed per group, and the osteosarcoma was collected for hematoxylin and eosin (H&E) staining. Pathological analysis reveal extensive karyopyknosis and necrosis in the Cy@Silk + NIR group, while there is no obvious necrosis in the other control groups (Figure 6C).

To completely evaluate the PTT effect of osteosarcoma, the tumor growth curve and survival rate of each group were continuously monitored (Figure 6D and E). In the group of saline or Cy@Silk nanoagents only, the tumors keep growing until death. While the tumor growth curve of the Saline + NIR group is improved but not obvious, and all mice died after 36 days. Obviously, the tumor volume continues to decrease or even disappear, and the life span is significantly prolonged in the Cy@Silk + NIR group. The results indicate that the Cy@Silk nanoparticles can be as promising biocompatible PTT agents for tumor treatment.

CONCLUSIONS

In summary, we successfully investigated and monitored the in vivo behaviors of self-assembled Cy@Silk nanoagents by multimodal photoacoustic/SPECT imaging. The results provided real time, noninvasive, sensitive, and whole-body 3D information about nanoagents' distribution in vivo. Both imaging techniques confirmed that the Cy@Silk nanoagents are mainly cleared from liver and metabolized to gallbladder, intestine, and ultimately feces. The Cy@Silk nanoagents have excellent in vivo cycle time, biocompatible and tumor enrichment efficiency, which can be as an excellent multimodal imaging probe with tumor targeting. Due to the excellent photothermal conversion and tumor targeting efficiency, the Cy@Silk nanoagents have been successfully applied to in vivo PTT of osteosarcoma. Potentially, design strategy of this paper is believed to be helpful for rational design and screening of nanoagents in biomedical applications and clinical translations.

ASSOCIATED CONTENT

Supporting Information

The Supporting Information is available free of charge on the ACS Publications website.

AUTHOR INFORMATION

Corresponding Author

* E-mail: wangyongac@gmail.com (Y. Wang)

ORCID

Yong Wang: 0000-0003-4061-7956

Author Contributions

Ŧ These authors contributed equally to the work.

REFERENCES

(1) Chen, H.; Zhang, W.; Zhu, G.; Xie, J.; Chen, X. Rethinking cancer nanotheranostics. *Nat. Rev. Mater.* **2017**, *2*, 17024.

(2) Wang, L.; Yan, L.; Liu, J.; Chen, C.; Zhao, Y. Quantification of Nanomaterial/Nanomedicine Trafficking in Vivo. *Anal. Chem.* **2018**, *90*, 589-614.

(3) Chen, C.; Li, Y. F.; Qu, Y.; Chai, Z.; Zhao, Y. Advanced nuclear analytical and related techniques for the growing challenges in nanotoxicology. *Chem. Soc. Rev.* **2013**, *42*, 8266-8303.

(4) Li, C.; Li, F.; Zhang, Y.; Zhang, W.; Zhang, X.-E.; Wang, Q. Real-Time Monitoring Surface Chemistry-Dependent In Vivo Behaviors of Protein Nanocages via Encapsulating an NIR-II Ag$_2$S Quantum Dot. *ACS Nano* **2015**, *9*, 12255-12263.

(5) Zhao, Z.; Wang, X.; Zhang, Z.; Zhang, H.; Liu, H.; Zhu, X.; Li, H.; Chi, X.; Yin, Z.; Gao, J. Real-Time Monitoring of Arsenic Trioxide Release and Delivery by Activatable T1 Imaging. *ACS Nano* **2015**, *9*, 2749-2759.

(6) Zhu, X.; Chi, X.; Chen, J.; Wang, L.; Wang, X.; Chen, Z.; Gao, J. Real-Time Monitoring in Vivo Behaviors of Theranostic Nanoparticles by Contrast-Enhanced T1 Imaging. *Anal. Chem.* **2015**, *87*, 8941-8948.

(7) Ali, Z.; Abbasi, A. Z.; Zhang, F.; Arosio, P.; Lascialfari, A.; Casula, M. F.; Wenk, A.; Kreyling, W.; Plapper, R.; Seidel, M.; Niessner, R.; Knöll, J.; Seubert, A.; Parak, W. J. Multifunctional Nanoparticles for Dual Imaging. *Anal. Chem.* **2011**, *83*, 2877-2882.

(8) Smith, B. R.; Gambhir, S. S. Nanomaterials for In Vivo Imaging. *Chem. Rev.* **2017**, *117*, 901-986.

(9) Heinzmann, K.; Carter, L. M.; Lewis, J. S.; Aboagye, E. O. Multiplexed imaging for diagnosis and therapy. *Nat. Biomed. Eng.* **2017**, *1*, 697-713.

(10) Dean-Ben, X. L.; Gottschalk, S.; Mc Larney, B.; Shoham, S.; Razansky, D. Advanced optoacoustic methods for multiscale imaging of in vivo dynamics. *Chem. Soc. Rev.* **2017**, *46*, 2158-2198.

(11) Weber, J.; Beard, P. C.; Bohndiek, S. E. Contrast agents for molecular photoacoustic imaging. *Nat. Methods* **2016**, *13*, 639-650.

(12) Yun, S. H.; Kwok, S. J. J. Light in diagnosis, therapy and surgery. *Nat. Biomed. Eng.* **2017**, *1*, 0008.

(13) Guo, Z.; Gao, M.; Song, M.; Li, Y.; Zhang, D.; Xu, D.; You, L.; Wang, L.; Zhuang, R.; Su, X.; Liu, T.; Du, J.; Zhang, X. Superfluorinated PEI Derivative Coupled with [99mTc] for ASGPR Targeted 19F MRI/SPECT/PA Tri-Modality Imaging. *Adv. Mater.* **2016**, *28*, 5898-5906.

(14) Wang, Y.; Wu, Y.; Liu, Y.; Shen, J.; Lv, L.; Li, L.; Yang, L.; Zeng, J.; Wang, Y.; Zhang, L. W.; Li, Z.; Gao, M.; Chai, Z. BSA-Mediated Synthesis of Bismuth Sulfide Nanotheranostic Agents for Tumor Multimodal Imaging and Thermoradiotherapy. *Adv. Funct. Mater.* **2016**, *26*, 5335-5344.

(15) Tian, Y.; Jiang, X.; Chen, X.; Shao, Z.; Yang, W. Doxorubicin-Loaded Magnetic Silk Fibroin Nanoparticles for Targeted Therapy of Multidrug-Resistant Cancer. *Adv. Mater.* **2014**, *26*, 7393-7398.

(16) Huang, W.; Ling, S.; Li, C.; Omenetto, F. G.; Kaplan, D. L. Silkworm silk-based materials and devices generated using bio-nanotechnology. *Chem. Soc. Rev.* **2018**, *47*, 6486-6504.

(17) Chen, Q.; Liu, Z. Albumin Carriers for Cancer Theranostics: A Conventional Platform with New Promise. *Adv. Mater.* **2016**, *28*, 10557-10566.

(18) Liu, Z.; Chen, X. Simple bioconjugate chemistry serves great clinical advances: albumin as a versatile platform for diagnosis and precision therapy. *Chem. Soc. Rev.* **2016**, *45*, 1432-1456.

(19) Jung, H. S.; Verwilst, P.; Sharma, A.; Shin, J.; Sessler, J. L.; Kim, J. S. Organic molecule-based photothermal agents: an expanding photothermal therapy universe. *Chem. Soc. Rev.* **2018**, *47*, 2280-2297.

(20) Wongpinyochit, T.; Uhlmann, P.; Urquhart, A. J.; Seib, F. P. PEGylated Silk Nanoparticles for Anticancer Drug Delivery. *Biomacromolecules* **2015**, *16*, 3712-3722.

(21) Wang, Y.; Yang, T.; Ke, H.; Zhu, A.; Wang, Y.; Wang, J.; Shen, J.; Liu, G.; Chen, C.; Zhao, Y.; Chen, H. Smart Albumin-Biomineralized Nanocomposites for Multimodal Imaging and Photothermal Tumor Ablation. *Adv. Mater.* **2015**, *27*, 3874-3882.

(22) Xu, Z.; Wang, Y.; Han, J.; Xu, Q.; Ren, J.; Xu, J.; Wang, Y.; Chai, Z. Noninvasive Multimodal Imaging of Osteosarcoma and Lymph Nodes Using a [99mTc]-Labeled Biomineralization Nanoprobe. *Anal. Chem.* **2018**, *90*, 4529-4534.

(23) Wang, Q.; Lv, L.; Ling, Z.; Wang, Y.; Liu, Y.; Li, L.; Liu, G.; Shen, L.; Yan, J.; Wang, Y. Long-Circulating Iodinated Albumin−Gadolinium Nanoparticles as Enhanced Magnetic Resonance and Computed Tomography Imaging Probes for Osteosarcoma Visualization. *Anal. Chem.* **2015**, *87*, 4299-4304.

(24) Duong, T.; Li, X.; Yang, B.; Schumann, C.; Albarqi, H. A.; Taratula, O.; Taratula, O. Phototheranostic nanoplatform based on a single cyanine dye for image-guided combinatorial phototherapy. *Nanomed. Nanotechnol. Biol. Med.* **2017**, *13*, 955-963.

(25) Yoon, H.-J.; Lee, H.-S.; Lim, J.-Y.; Park, J.-H. Liposomal Indocyanine Green for Enhanced Photothermal Therapy. *ACS Appl. Mater. Interfaces* **2017**, *9*, 5683-5691.

(26) Chu, K. F.; Dupuy, D. E. Thermal ablation of tumours: biological mechanisms and advances in therapy. *Nat. Rev. Cancer* **2014**, *14*, 199-208.

(27) Mitchell, M. J.; Jain, R. K.; Langer, R. Engineering and physical sciences in oncology: challenges and opportunities. *Nat. Rev. Cancer* **2017**, *17*, 659-675.

(28) Bourquin, J.; Milosevic, A.; Hauser, D.; Lehner, R.; Blank, F.; Petri-Fink, A.; Rothen-Rutishauser, B. Biodistribution, Clearance, and Long-Term Fate of Clinically Relevant Nanomaterials. *Adv. Mater.* **2018**, *30*, 1704307.

(29) Shi, J.; Kantoff, P. W.; Wooster, R.; Farokhzad, O. C. Cancer nanomedicine: progress, challenges and opportunities. *Nat. Rev. Cancer* **2017**, *17*, 20-37.

(30) Golombek, S. K.; May, J.-N.; Theek, B.; Appold, L.; Drude, N.; Kiessling, F.; Lammers, T. Tumor targeting via EPR: Strategies to enhance patient responses. *Adv. Drug Delivery Rev.* **2018**, *130*, 17-38.

(31) Lin, S.; Wang, Y.; Chen, Z.; Li, L.; Zeng, J.; Dong, Q.; Wang, Y.; Chai, Z. Biomineralized Enzyme-Like Cobalt Sulfide Nanodots for Synergetic Phototherapy with Tumor Multimodal Imaging Navigation. *ACS Sustainable Chem. Eng.* **2018**, *6*, 12061-12069.

Table of Contents

Cy@Silk Nanoagents

Dynamic Photoacoustic Imaging

Dynamic SPECT Imaging

Photothermal Imaging/Therapy